Downregulating PTBP1 fails to convert astrocytes into hippocampal neurons and to alleviate symptoms in Alzheimer's mouse models

Authors

Tiantian Guo[1#], Xinjia Pan[1#], Guangtong Jiang[1], Denghong Zhang[1], Jinghui Qi[1], Lin Shao[1], Zhanxiang Wang[1], Huaxi Xu[1,2*], Yingjun Zhao[1*]

Affiliations

[1]Center for Brain Sciences, the First Affiliated Hospital of Xiamen University, Institute of Neuroscience, Fujian Provincial Key Laboratory of Neurodegenerative Disease and Aging Research, School of medicine, Xiamen University, Xiamen, China.

[2]Institute for Brain Science and Disease, Chongqing Medical University, Chongqing, China.

[#]These authors contributed equally.

*Correspondence:

Huaxi.Xu@MolecularNeurodegeneration.org;

yjzhao@xmu.edu.cn

Abstract

Conversion of astroglia into functional neurons has been considered as a promising therapeutic strategy for neurodegenerative diseases. Recent studies reported that downregulation of the RNA binding protein, PTBP1, converts astrocytes into neurons in situ in multiple mouse brain regions, consequently improving pathological phenotypes associated with Parkinson's disease, RGC loss, and aging. Here, we demonstrate that PTBP1 downregulation using antisense oligonucleotides or an astrocyte specific AAV-mediated shRNA system fails to convert hippocampal astrocytes into neurons in WT, and β-amyloid (5×FAD) and tau (PS19) Alzheimer's disease (AD) mouse models, and fails to reverse synaptic/cognitive deficits and AD-associated pathology. Similarly, PTBP1 downregulation cannot convert astrocytes into neurons in the striatum and substantia nigra. Together, our study suggests that cell fate conversion strategy for neurodegenerative disease therapy through manipulating one single gene, such as PTBP1, warrants more rigorous scrutiny.

Introduction

Neuronal loss is the primary cause for functional deterioration in the central nervous system (CNS) in neurodegenerative diseases such as Parkinson's disease (PD) and Alzheimer's disease (AD) (Kalia & Lang, 2015; Mesulam, 1999). Replenishment of neurons is considered as an effective approach to restore CNS function. Two major regeneration strategies utilizing neuronal lineage cells have been developed so far: transplantation of exogenous iPSC-derived neuronal cells and activation of endogenous neurogenesis niche. However, transplantation of exogenous cells may induce immunological rejection and tumorigenesis (Olanow et al., 2003; Trounson & McDonald, 2015). Adult neurogenesis only occurs in a few small brain regions in rodent models, and whether it exists in humans remains controversial (Gage, 2019; Kempermann et al., 2018). In pursuing novel approaches for neuronal replenishment, attempts have been made to transdifferentiate residential glia cells into functional neurons (Chen et al., 2020; Grande et al., 2013; Guo et al., 2014; Lentini et al., 2021; Liu et al., 2015; Maimon et al., 2021; Matsuda et al., 2019; Mattugini et al., 2019; Niu et al., 2015; Qian et al., 2020; Tai et al., 2021; Torper et al., 2015; Zhou et al., 2020). The *in situ* glia-to-neuron conversion represents an ideal strategy for neuronal regeneration, because: (1) glial cells including astrocytes and microglia are over-proliferated and become reactive (this process was termed as gliosis), leading to neuroinflammation during neurodegeneration; (2) neurons can be regenerated from the excessive glia in designated brain regions where neuronal loss occurs.

Among the targets for converting astroglia into neurons, polypyrimidine tract-binding protein 1 (PTBP1) has attracted much attention, because downregulation of this single protein has been indicated to be sufficient to directly convert astrocytes into functional neurons with high efficiencies, within several weeks to months (Maimon et al., 2021; Qian et al., 2020; Zhou et al., 2020). Specifically, downregulation of PTBP1 by AAV-mediated shRNA system

or antisense oligonucleotides (ASO) converted midbrain astrocytes to dopaminergic neurons, and reversed motor deficits in a chemically induced PD mouse model (Qian et al., 2020). Similar motor function improvement was observed in the PD mice when striatal astrocytes were converted into functional neurons by CRISPR-CasRx-mediated PTBP1 downregulation (Zhou et al., 2020). In addition, injection of ASO targeting *Ptbp1* into cerebral spinal fluid (CSF) generated new functional cortical or hippocampal neurons in both young and aged mice (Maimon et al., 2021). Those results, should they sustain, would represent revolutionary advancement in therapeutics for neurodegenerative diseases.

In the current study, utilizing ASO and an astrocyte-restrictive AAV shRNA system, we examine whether the reported astrocyte-to-neuron conversion induced by PTBP1 downregulation can happen in the hippocampus and consequently rescue synaptic and cognitive impairments in AD-associated mouse models, namely amyloid and tau (neurofibrillary tangle) models, 5×FAD and PS19, respectively. In addition, we re-examine whether PTPB1 knockdown can efficiently convert astrocytes into neurons in the brain regions of substantia nigra and striatum, as previously reported.

Results

Downregulation of PTBP1 by ASO fails to promote the generation of neurons in mouse hippocampus

Because there is a great potential for ASO in clinical applications (Leavitt & Tabrizi, 2020; Miller et al., 2020; Miller et al., 2013), we first tested the effect of *Ptbp1* ASO (with the same nucleotide sequence as reported in (Qian et al., 2020) on neuronal generation. Two weeks after mouse hippocampal injection of a FAM-labeled ASO targeting *Ptbp1* (*Ptbp1*-ASO), we observed FAM signals in mostly NeuN$^+$ and to a much lesser extent GFAP$^+$ cells near the injection site

106 (**Figure 1—figure supplement 1A**), indicating the lack of astrocytic specificity
107 for ASO delivery. *Ptbp1*-ASO injection resulted in a significant reduction, but
108 incomplete elimination of PTBP1 immunofluorescent (IF) intensities in GFAP$^+$
109 cells (**Figure 1—figure supplement 1**, **B** and **C**); however, the number of cells
110 labeled with doublecortin X (DCX), a marker for neural progenitor cells and
111 immature neurons, and the area labeled by mature neuronal marker NeuN are
112 indistinguishable between the *Ptbp1*-ASO and the control groups (**Figure 1—**
113 **figure supplement 1, D** to **F**). These data suggest that downregulation of
114 PTBP1 by ASO cannot promote the generation of both immature and mature
115 neurons.

116 **Knockdown of PTBP1 by an astrocyte-restrictive AAV shRNA fails to**
117 **convert hippocampal astrocytes into neurons *in vivo***

118 AAV driven by specific promoters has been widely used to efficiently deliver
119 genes or DNA fragments including shRNAs into particular types of CNS cells.
120 We constructed an *hGFAP* promoter-driven AAV vector, which comprises a
121 mCherry reporter and a *Ptbp1*-targeting shRNA in a miR30 cassette (**Figure**
122 **1A**). A modified longer form of *hGFAP* promoter was used to ensure the
123 specificity of astrocytic expression, as many serotypes of the AAV driven by the
124 short form *hGFAP* promoter have been reported to having leaky expression in
125 non-astrocytic cells (Wang et al., 2021). The knockdown efficiency of three AAV
126 shRNA viruses was compared with the control AAV scramble virus in primary
127 astrocytic cultures. Because of the highest knockdown efficiency of AAV-GFAP-
128 sh*Ptbp1*-1 (**Figure 1**, **B** and **C**) (nucleotide sequence of the shRNA is identical
129 to that used in (Qian et al., 2020)), it was chosen and designated as AAV-
130 sh*Ptbp1* or sh*Ptbp1* for all subsequent experiments.

131 We next transduced AAV-sh*Ptbp1* unilaterally into the right hippocampal
132 dentate gyrus, and AAV-scramble control in the left dentate gyrus, of adult WT
133 mice (**Figure 1D**). Two weeks after the transduction, both sides showed

134 restricted mCherry expression in GFAP$^+$ astrocytes in the dentate gyrus and
135 the nearby areas (**Figure 1, E** to **G**). IF staining for PTBP1 showed that AAV-
136 sh*Ptbp1* achieved nearly complete depletion of PTBP1 in mCherry$^+$ cells, and
137 consequently dramatic reduction in the number of PTBP1$^+$mCherry$^+$ cells, when
138 compared to the control side (**Figure 1, H** and **I**). These results demonstrate
139 that AAV-sh*Ptbp1* can rapidly, efficiently, and specifically knockdown PTBP1 in
140 the hippocampal astrocytes *in vivo*. Nevertheless, AAV-sh*Ptbp1* yielded only
141 handful and neglectable numbers of NeuN$^+$mCherry$^+$ cells, which are similar to
142 AAV-scramble control (**Figure 1, J** and **K**). DCX$^+$mCherry$^+$ cells were
143 undetectable, whereas the numbers of DCX$^+$ cells were comparable in the
144 knockdown and control groups (**Figure 1, J, L** and **M**). Our data clearly show
145 that suppression of PTBP1 expression cannot convert astrocytes into either
146 immature or mature neurons.

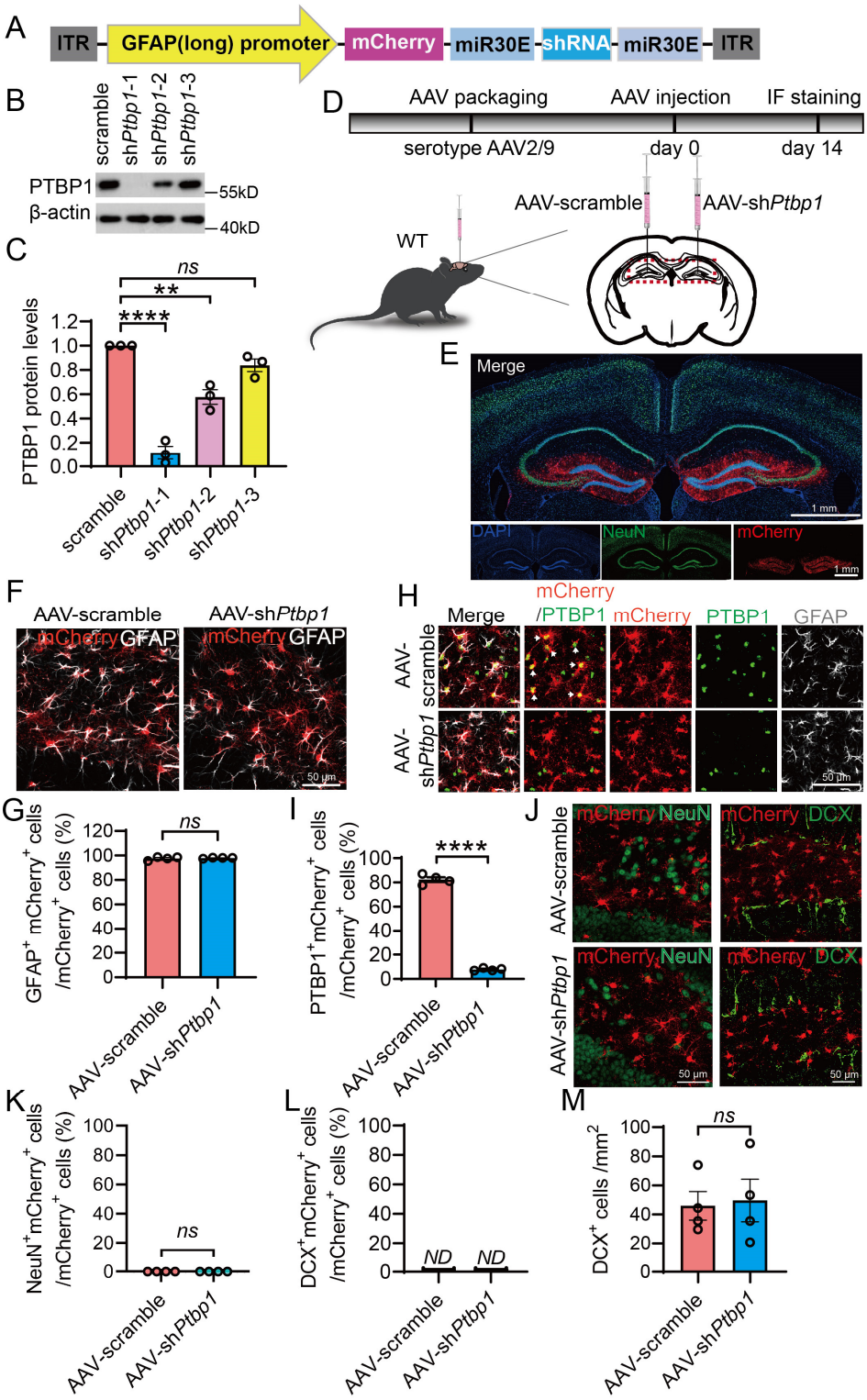

Figure 1. Specific knockdown of PTBP1 in astrocytes fails to convert hippocampal astrocytes into neurons in WT mice

(**A**) Schematic of the AAV-shRNA vector used in this study. (**B** and **C**) Western blot analysis of PTBP1 expression in mouse primary astrocytes 7 days post

152 AAV transduction. (B) Representative PTBP1 blots, (C) quantification. n = 3
153 independent experiments, one-way ANOVA with Tukey's multiple
154 comparisons. (**D**) Flow chart of study design to assess PTBP1
155 downregulation in mouse hippocampus. (**E**) Confocal images of the mouse
156 hippocampus and cortex 2 weeks after the AAV injection. (**F** and **G**) Confocal
157 analysis of mCherry expression in GFAP$^+$ cells. (F) Representative images,
158 (G) quantification. n = 4 animals, unpaired t-test. (**H** and **I**) Confocal analysis
159 of PTBP1 expression in mCherry$^+$ cells. (H) Representative images, (I)
160 quantification. n = 4 animals, unpaired t-test. (**J** to **M**) Confocal analysis of
161 fluorescent cells. (J) Representative images, (K-M) quantification. n = 4
162 animals, unpaired t-test. All quantified data are represented as mean ± SEM;
163 **p <0.01; ****p <0.0001; *ns*, not significant; *ND*, undetectable. Figure 1—
164 source data 1 to 7, source data for Figure 1B, 1C, 1G, 1I, 1K, 1L, 1M.
165

166 **Sustained downregulation of PTBP1 fails to convert hippocampal**
167 **astrocytes into neurons in an amyloid AD mouse model**

168 Next, we investigated whether a long-term and continuous PTBP1
169 downregulation can enhance neuronal generation in 5×FAD mice, a widely
170 used AD mouse model with progressive amyloid-β (Aβ) pathology, synaptic and
171 cognitive impairments (Guo et al., 2020). The long-term knockdown of PTBP1
172 strategy was based on the fact that the astrocyte-to-neuron conversion as well
173 as the pathogenesis of most neurodegenerative diseases such as AD and PD
174 are progressive and chronic. We injected AAV-sh*Ptbp1* or AAV-scramble
175 bilaterally into the hippocampus of 5×FAD and WT control mice at ~5.5 months
176 of age, and performed IF analyzes at 1 and up to 3 months after the
177 transduction. AAV-sh*Ptbp1* markedly reduced the expression of PTBP1 in
178 mCherry$^+$ cells, when compared to the AAV-scramble group (**Figure 2, A** and
179 **B,** and **Figure 2—figure supplement 1, A** and **B**). However, only a neglectable

fraction of NeuN$^+$mCherry$^+$ cells were observed, whereas the vast majority of mCherry$^+$ cells are GFAP$^+$ astrocytes (**Figure 2, C** to E, and **Figure 2—figure supplement 1, C** to **E**). In addition, NeuN$^+$ areas did not vary between AAV-sh*Ptbp1* and AAV-scramble groups (**Figure 2, C** and **F,** and **Figure 2—figure supplement 1, C** and **F**). Further, AAV-sh*Ptbp1* failed to reverse the over-proliferation of GFAP$^+$ astrocytes and the reduction of DCX$^+$ cells in 5×FAD mice (**Figure 2, C** and **G** to **I,** and **Figure 2—figure supplement 1, C** and **G to I**), two phenomena that have been reported (Demars et al., 2010; Perez-Nievas & Serrano-Pozo, 2018; Zaletel et al., 2018). DCX$^+$mCherry$^+$ cells were completely undetectable in all groups (**Figure 2, H** and **J** and **Figure 2—figure supplement 1, H** and **J**). Together, these results demonstrate that sustained downregulation of PTBP1 in the hippocampus also fails to convert astrocytes into neurons in 5×FAD mice.

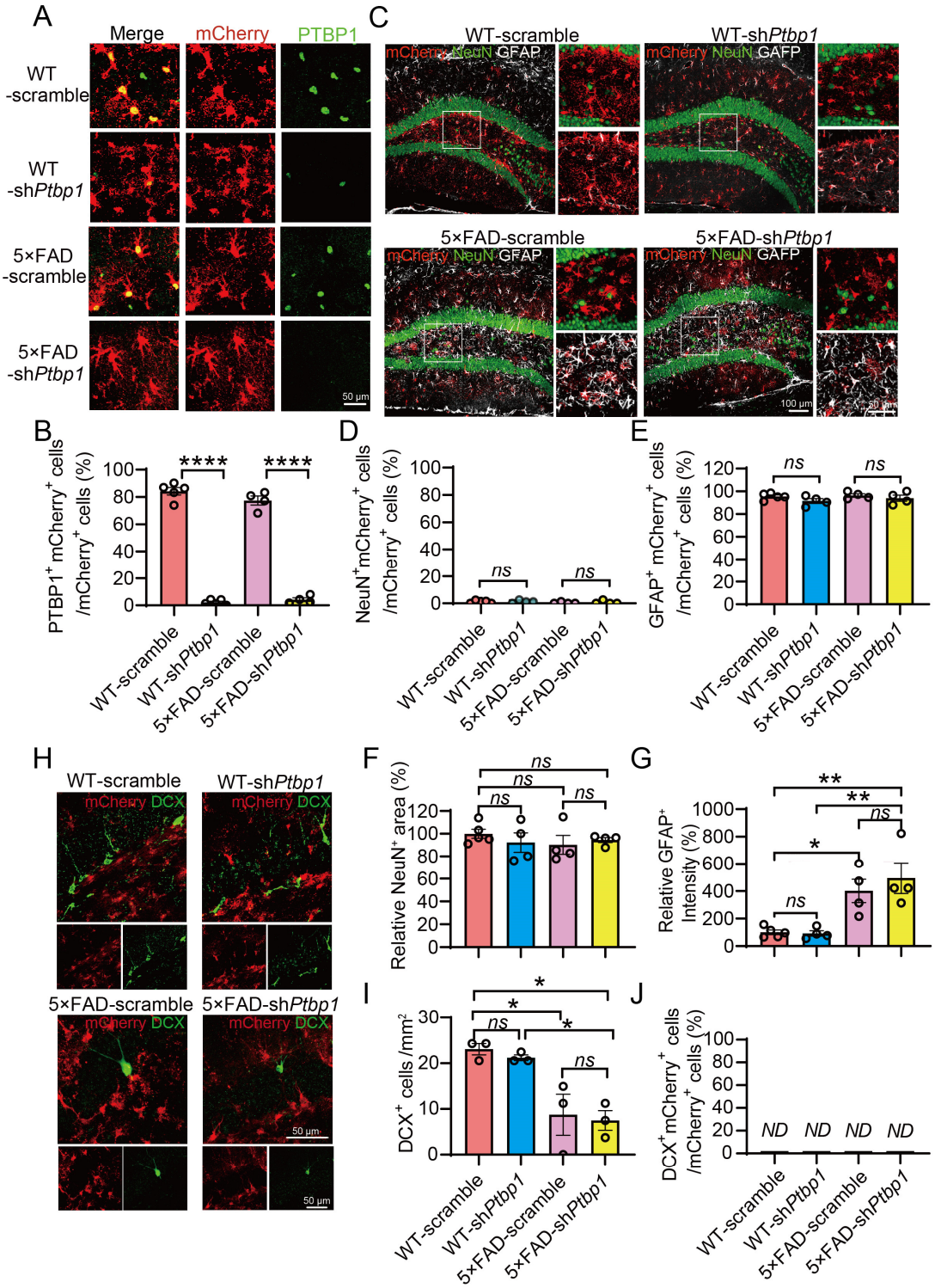

Figure 2. Downregulation of PTBP1 is not able to convert astrocytes into neurons in the hippocampus of 5×FAD mice

(**A** and **B**) Confocal analysis of PTBP1 expression in mCherry⁺ cells in the hippocampus of 5×FAD and WT control mice 3 months after sh*Ptbp1* or the

198 scramble control AAV transduction. (A) Representative images, (B)
199 quantification. n = 4 to 5 animals, unpaired t-test. (**C** to **G**) Confocal analysis of
200 fluorescent cells. (C) Representative images, (D-G) quantification. n = 4 to 5
201 animals, one-way ANOVA with Tukey's multiple comparisons. (**H** to **J**) Confocal
202 analysis of mCherry^{+} cells and DCX^{+} cells. (H) Representative images (I and J)
203 quantification. n = 3 animals per group, one-way ANOVA with Tukey's multiple
204 comparisons. All quantified data are represented as mean ± SEM; *p <0.05; **p
205 <0.01; ****p <0.0001; *ns*, not significant; *ND*, undetectable. Figure 2—source
206 data 1 to 7, source data for Figure 2B, 2D, 2E, 2F, 2G, 2I, 2J.
207

208 **PTBP1 downregulation cannot alleviate Aβ-associated synaptic and**
209 **cognitive deficits and pathologies in AD mice**

210 The ultimate goal for neuronal regeneration is to restore brain functions which
211 are impaired in neurodegeneration. We performed behavioral tests to evaluate
212 cognitive functions of the mice after AAV-mediated PTBP1 knockdown. In the
213 Morris water maze test, AAV-sh*Ptbp1* failed to alleviate the deficits of spatial
214 memory in 5×FAD mice in the training and probe test phases (**Figure 3, A** and
215 **B**). Similarly, the novel object recognition (NOR) test showed that comparing to
216 the WT control mice, 5×FAD mice spent less time on the novel object, and AAV-
217 sh*Ptbp1* was unable to reverse this deficit (**Figure 3C**). As expected, AAV-
218 sh*Ptbp1* also failed to rescue impairments in long-term potentiation (LTP) and
219 synaptophysin (SYP) /PSD95 labeled synaptic clusters in 5×FAD mice (**Figure**
220 **3, D** to **G**). Additionally, amyloid deposition in the hippocampus of 5×FAD mice
221 was not altered after PTBP1 downregulation (**Figure 3, H** and **I**). Taken together,
222 PTBP1 downregulation can neither restore synaptic and cognitive function, nor
223 reduce amyloid pathology in 5×FAD mice.

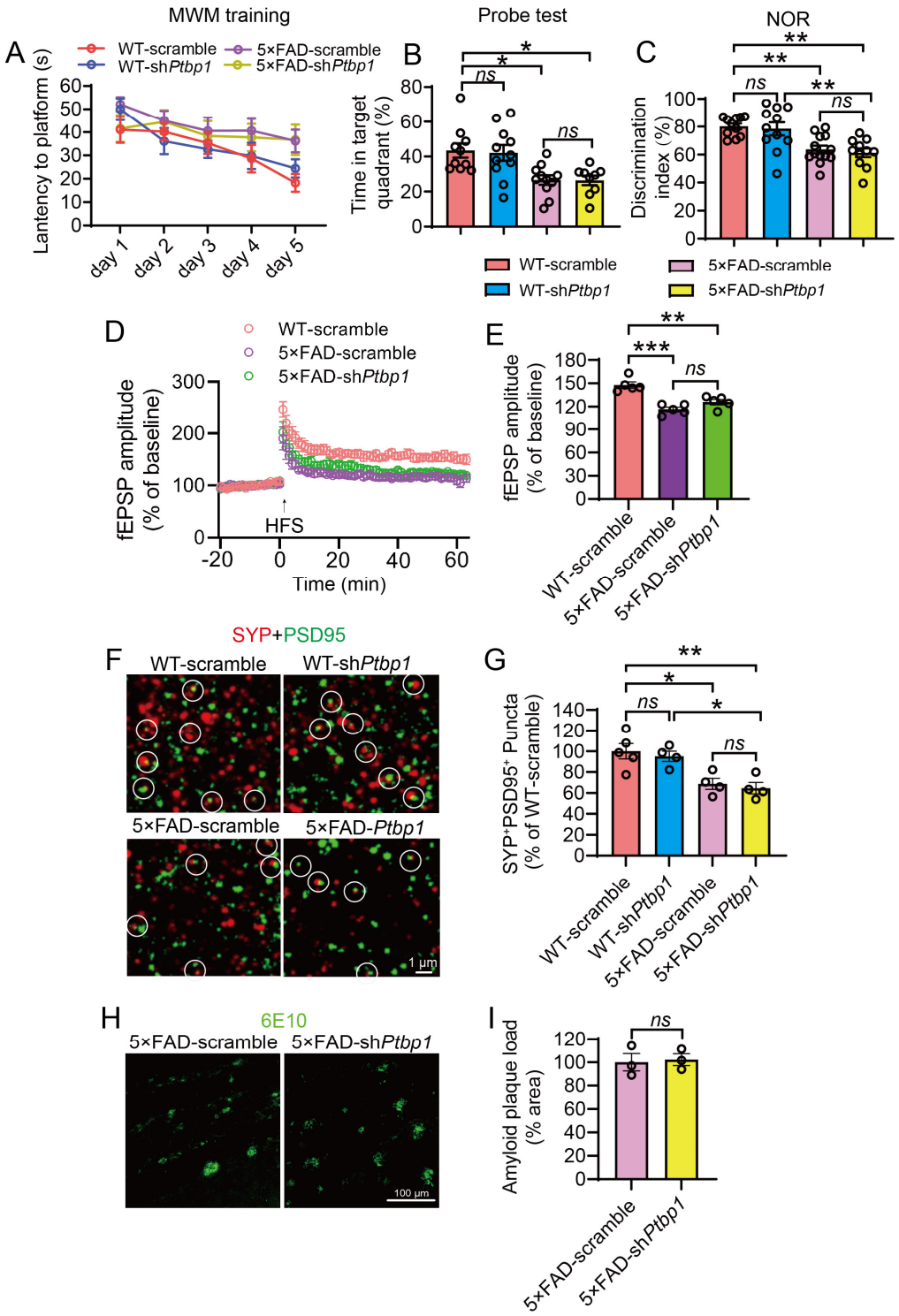

Figure 3. Downregulation of PTBP1 in the hippocampus fails to attenuate cognitive and synaptic deficits as well as Aβ deposition in 5×FAD mice

(**A** and **B**) MWM analysis of 5×FAD and WT control mice 2.5 months after sh*Ptbp1* or the scramble control AAV transduction. (A) The Latency to find the

229 hidden platform during the training phase, (B) time spent in the target quadrant
230 in the probe test. n = 9 to 11 animals, one-way ANOVA with Tukey's multiple
231 comparisons. (**C**) Quantification of discrimination indexes in the NOR test of the
232 experimental mouse. n = 11 to 13 animals, one-way ANOVA with Tukey's
233 multiple comparisons. (**D** and **E**) Electrophysiological analysis of LTP. (D)
234 Recordings of hippocampal LTP induced by high-frequency stimulation (HFS),
235 (E) quantification of the field excitatory post synaptic potentials (fEPSP) during
236 the last 10 min of LTP recording. n = 5 brain slices from 4 animals per group,
237 one-way ANOVA with Tukey's multiple comparisons. (**F** and **G**) Confocal
238 analysis of $SYP^{+}PSD95^{+}$ synaptic puncta. (F) Representative images, (G)
239 quantification. n = 4 to 5 animals, one-way ANOVA with Tukey's multiple
240 comparisons. (**H** and **I**) Confocal analysis of 6E10 (Aβ antibody) stained
241 amyloid deposits. (H) Representative images, (I) quantification. n = 3 animals
242 per group, unpaired t-test. All quantified data are represented as mean ± SEM;
243 *p <0.05; **p <0.01; ***p <0.001 *ns*, not significant. Figure 3—source data 1 to
244 7, source data for Figure 3A, 3B, 3C, 3D, 3E, 3G, 3I.
245

246 **Knockdown of PTBP1 fails to induce the hippocampal astrocyte-to-**
247 **neuron conversion and to improve cognitive function in tau transgenic**
248 **mice**

249 Tau pathology has been linked to the degree of dementia and considered to
250 play a causal role in neuronal loss in tauopathies including AD (Fu et al., 2017;
251 Guo et al., 2020). We therefore assessed the PTPB1 knockdown strategy in
252 tau transgenic PS19 mice that develop neuronal loss and brain atrophy starting
253 from 9 month (Yoshiyama et al., 2007). AAV-sh*Ptbp1* or AAV-scramble viruses
254 were injected bilaterally into the hippocampus of 8-month-old PS19 and WT
255 mice. Similar to the 5×FAD mice tested above, the expression of PTBP1 was
256 dramatically reduced in $mCherry^{+}$ cells 3 months post AAV-sh*Ptbp1*

257 transduction (**Figure 4, A** and **B**). mCherry fluorescent signals were detected
258 mostly in GFAP$^+$ astrocytes, sparsely in NeuN$^+$ neurons, and were undetectable
259 in DCX$^+$ cells, in both AAV-sh*Ptbp1* and AAV-scramble groups (**Figure 4, C** to
260 **E, H** and **I**). Consistent with the previous reports (Yoshiyama et al., 2007), we
261 expectedly observed the apparent loss of NeuN$^+$ mature neurons and DCX$^+$
262 neuronal progenitors, as well as increased GFAP$^+$ astrocytes in PS19 mice, all
263 of which, however, remained completely unaffected following the efficient
264 PTBP1 downregulation (**Figure 4, C, F, G, H** and **J**).

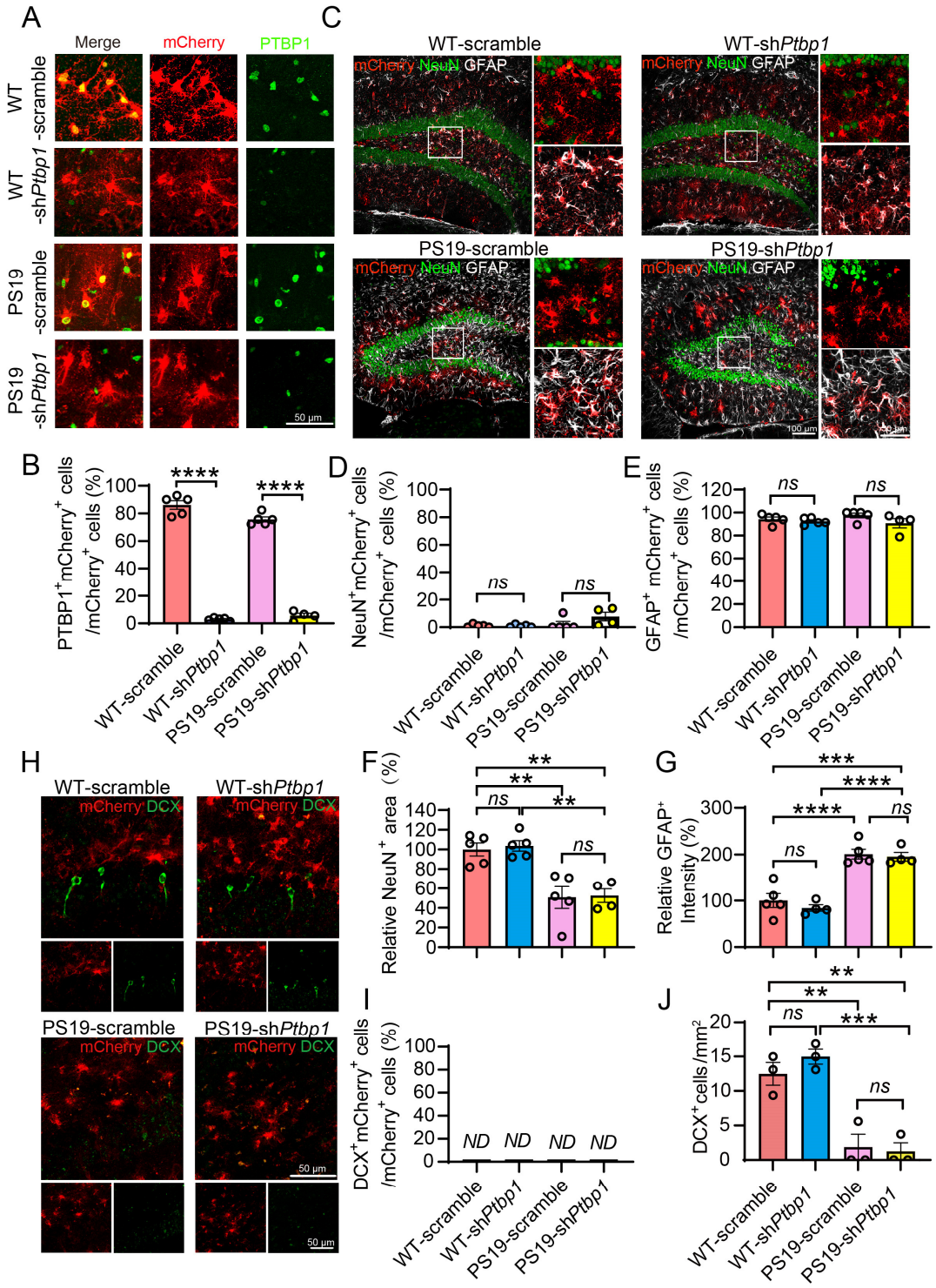

Figure 4. Knockdown of PTBP1 cannot convert astrocytes into neurons in the hippocampus of PS19 mice

(**A** and **B**) Confocal analysis of PTBP1 expression in mCherry⁺ cells in the hippocampus of PS19 and WT control mice 3 months after sh*Ptbp1* or the

270 scramble control AAV transduction. (A) Representative images, (B)
271 quantification. n = 4 to 5 animals, unpaired t-test. (**C** to **G**) Confocal analysis of
272 fluorescent cells. (C) Representative images, (D-G) quantification. n = 4 to 5
273 animals, one-way ANOVA with Tukey's multiple comparisons. (**H** to **J**) Confocal
274 analysis of mCherry^{+} cells and DCX^{+} cells. (H) Representative images, (I and
275 J) quantification. n = 3 animals per group, one-way ANOVA with Tukey's
276 multiple comparisons. All quantified data are represented as mean ± SEM; **p
277 <0.01; ***p <0.001; ****p <0.0001; *ns*, not significant; *ND*, undetectable. Figure
278 4—source data 1 to 7, source data for Figure 4B, 4D, 4E, 4F, 4G, 4I, 4J.
279
280 Cognitive function of PS19 and WT mice transduced with AAV-sh*Ptbp1* or
281 AAV-scramble were also assessed. In the NOR test, PS19 mice spent
282 significantly less time on the novel object, when compared to the WT control
283 groups; and downregulation of PTBP1 did not improve this performance
284 (**Figure 5A**). We next employed contextual fear conditioning (CFC) test to
285 examine memory decay and found that AAV-sh*Ptbp1* failed to rescue the
286 deficits of PS19 mice in freezing behaviors, when examined two weeks after
287 the initial electric shock (**Figure 5B**). In addition, we surveyed synapses and
288 tau pathology in PS19 mice, and found that loss of SYP^{+}PSD95^{+} synaptic
289 clusters and the presence of AT8^{+} phosphor-tau deposition remained and were
290 not alleviated by PTBP1 knockdown (**Figure 5, C** to **F**). The levels of tau
291 phosphorylated at T181 site were also not altered (data not shown).

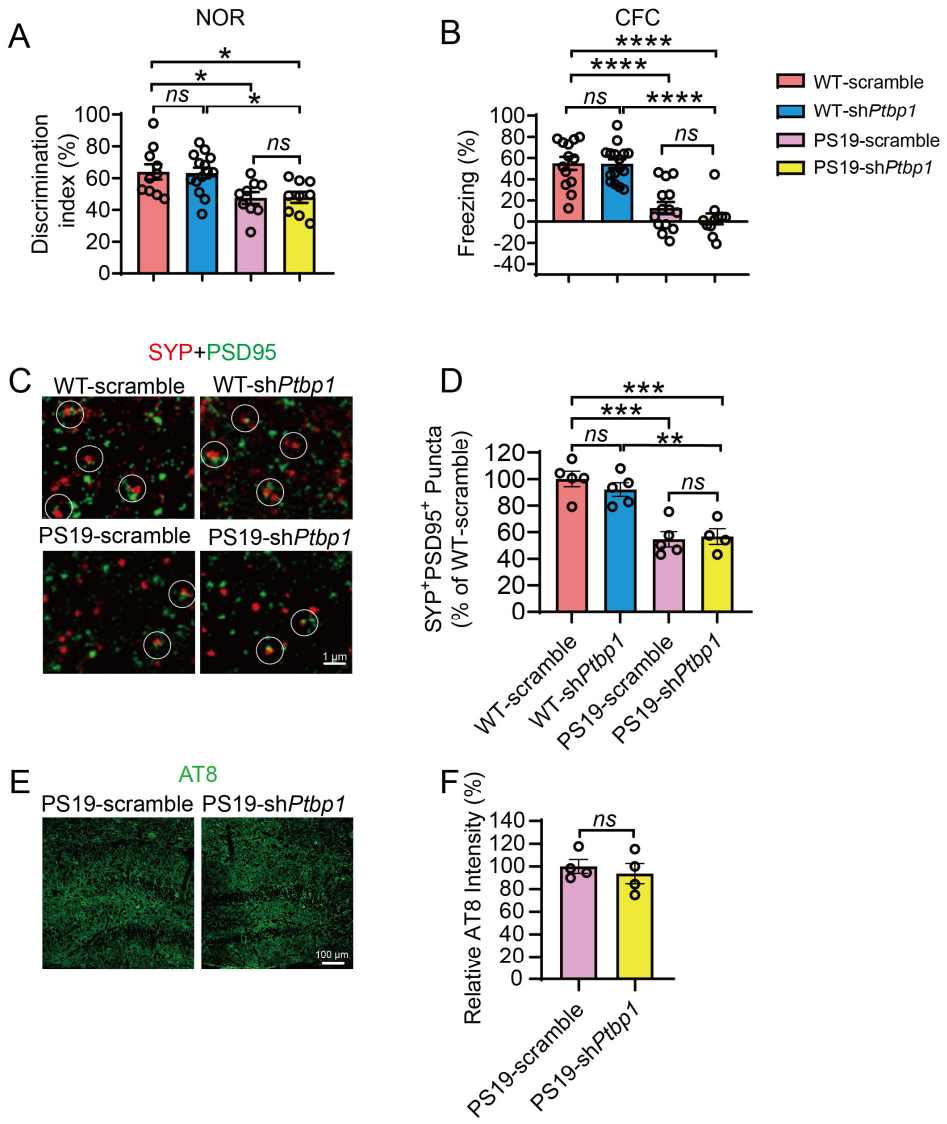

Figure 5. Downregulation of PTBP1 in the hippocampus fails to attenuate cognitive and synaptic deficits as well as tau pathology in PS19 mice

(**A**) Quantification of discrimination indexes in the NOR test of PS19 and WT control mice 2.5 month after the sh*Ptbp1* or the scramble control AAV transduction. n = 9 to 14 animals, one-way ANOVA with Tukey's multiple comparisons. (**B**) Analysis of the freezing behavior of the experimental mouse during the CFC test. n= 11 to 16 animals, one-way ANOVA with Tukey's multiple comparisons. (**C** and **D**) Confocal analysis of $SYP^{+}PSD95^{+}$ synaptic puncta. (C) Representative images, (D) quantification. n = 4 to 5 animals, one-way ANOVA with Tukey's multiple comparisons. (**E** and **F**) Confocal analysis of AT8

303 (phospho-tau antibody) stained tau pathology. (E) Representative images, (F)
304 quantification. n= 4 animals per group, unpaired t-test. All quantified data are
305 represented as mean ± SEM; *p <0.05; **p <0.01; ***p <0.001; ****p <0.0001;
306 *ns*, not significant. Figure 5—source data 1 to 4, source data for Figure 5A, 5B,
307 5D, 5F.
308
309 Together, our results clearly show that downregulation of PTBP1 in
310 hippocampal astrocytes fails to convert astrocytes into neurons, and
311 consequently are unable to improve cognitive function in mice under either
312 physiological or pathological conditions associated with AD.
313
314 **Downregulation of PTBP1 fails to convert astrocytes into neurons in**
315 **either striatum or substantia nigra of mice**
316 To investigate whether the brain-region specificity exists for the presumed
317 astroglia-to-neuron conversion induced by PTBP1 downregulation, we injected
318 AAV-sh*Ptbp1* or AAV-scramble viruses into the striatum or substantia nigra of
319 the adult mice, the two brain regions in which a successful astrocyte-to-neuron
320 conversion by downregulating PTBP1 has been claimed (Qian et al., 2020;
321 Zhou et al., 2020). In our study, similar to the hippocampus, astrocytic PTBP1
322 expression was nearly completely downregulated by AAV-sh*Ptbp1* in the
323 striatum 1 or 2 months after the viral injection (**Figure 6, A** to **C**). However, we
324 found that only a neglectable portion of mCherry$^+$ cells were NeuN$^+$, while most
325 of mCherry$^+$ cells were GFAP$^+$ (**Figure 6, D** to **F**), indicative of a complete failure
326 of astrocyte-to-neuron conversion. In addition, the numbers of NeuN$^+$ or GFAP$^+$
327 cells near the injection site were indistinguishable between AAV-sh*Ptbp1* and
328 the control AAV-scramble groups (**Figure 6, G** to **H**).

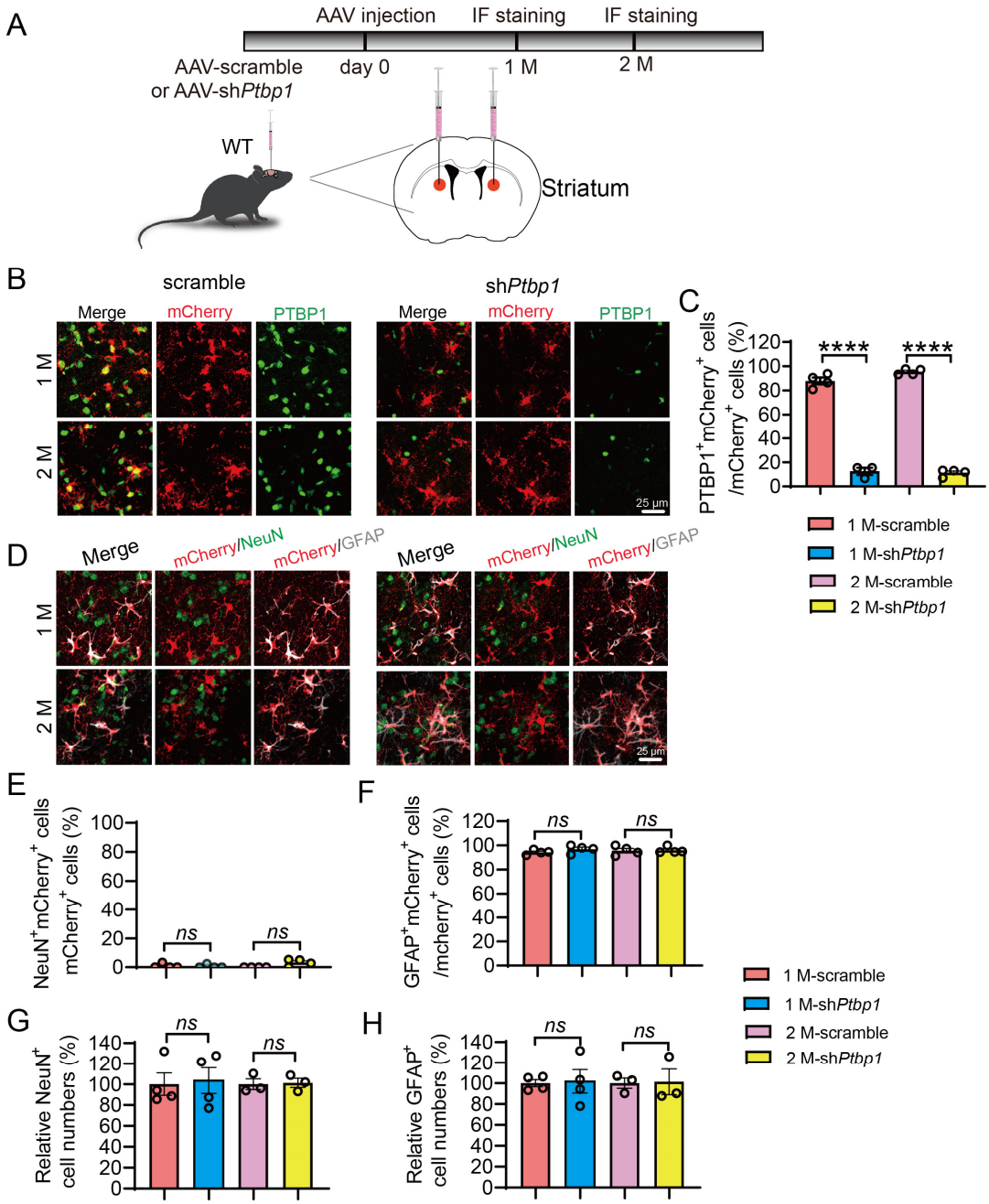

Figure 6. Knockdown of PTBP1 cannot convert astrocytes into neurons in the mouse striatum

(**A**) Schematic of study design. (**B** and **C**) Confocal analysis of PTBP1 expression in mCherry⁺ cells. (B) Representative images, (C) quantification. n = 3 to 4 animals, one-way ANOVA with Tukey's multiple comparisons. (**D** to **H**) Confocal analysis of fluorescent cells. (D) Representative images, (E-H) Quantification. n = 3 to 4 animals, one-way ANOVA with Tukey's multiple

comparisons. All quantified data are represented as mean ± SEM; ****p <0.0001; *ns*, not significant. Figure 6—source data 1 to 5, source data for Figure 5C, 5E, 5F, 5G, 5H.

Similar results were obtained in the substantia nigra region: an efficient knockdown of PTBP1 in astrocytes did not result in any significant differences in the numbers of $NeuN^{+}mCherry^{+}$, $GFAP^{+}mCherry^{+}$, $NeuN^{+}$ and $GFAP^{+}$ cells, when compared to the scramble control group (**Figure 7, A** to **H**). Together, our data clearly demonstrate that downregulation of PTBP1 is unable to convert astrocytes into neurons in all brain regions tested including the hippocampus, the striatum and the substantia nigra.

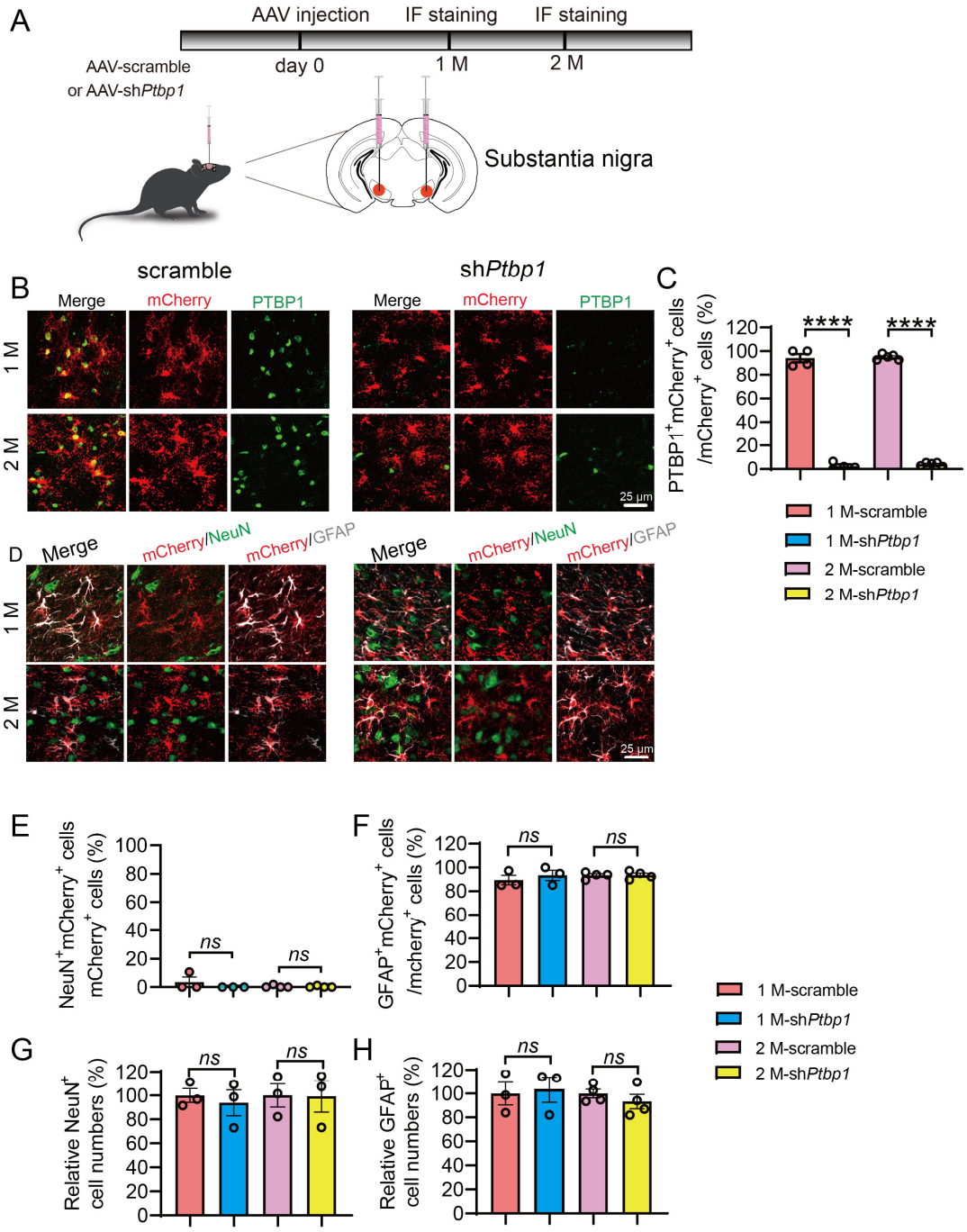

Figure 7. Downregulation of PTBP1 cannot convert astrocytes into neurons in the mouse substantia nigra

(**A**) Schematic of study design. (**B** and **C**) Confocal analysis of PTBP1 expression in mCherry⁺ cells. (B) Representative images, (C) quantification. n = 4 to 5 animals, one-way ANOVA with Tukey's multiple comparisons. (**D** to **H**) Confocal analysis of fluorescent cells. (D) Representative images, (E-H)

355 quantification. n = 3 to 4 animals, one-way ANOVA with Tukey's multiple
356 comparisons. All quantified data are represented as mean ± SEM; ****p
357 <0.0001; *ns*, not significant. Figure 7—source data 1 to 5, source data for Figure
358 7C, 7E, 7F, 7G, 7H.
359

360

361 **Discussion**

362 Having efficiently downregulated PTBP1 in the astrocytes in combination with
363 cell lineage and transcriptomic analyses, we fail to observe any glia-to-neuron
364 conversion induced by PTBP1 knockdown in multiple rodent brain regions at
365 different ages, under either physiological or pathological conditions associated
366 with AD. Similar to what we have found, a recent study also failed to replicate
367 the reported astrocyte-to-neuron conversion as a result of PTBP1 knockdown
368 (Wang et al., 2021). In the same study, Wang et al observed a dramatically
369 increased number of $NeuN^{+}mCherry^{+}$ cells in the mouse brain transduced with
370 astrocyte-restrictive AAV expressing mCherry reporter and NeuroD1. They
371 therefore employed stringent lineage tracing strategies to investigate the origin
372 of the increased $NeuN^{+}mCherry^{+}$ cells, and revealed that they are in fact
373 endogenous neurons that were experimentally labeled with mCherry due to
374 altered cell type specificity of the AAV virus induced by NeuroD1
375 overexpression. Because we found no evidence for neuronal generation
376 induced by PTBP1 downregulation, it is therefore unnecessary to perform the
377 lineage tracing analysis.

378 The discrepancies between the findings from Fu-Yang labs and our and
379 Zhang labs are not likely due to differentially viral toxicities, because similar
380 titers of AAV were used in all studies; instead, the differential leakage of
381 astrocytic labeling systems would be more likely. Our AAV driven by the long

form *hGFAP* promoter showed extremely low leaky expression in neurons. Apparent neuronal leakage of Cre expression in neuronal cells has been well documented in the *mGfap-Cre* line (Wang et al., 2021), which was utilized in Qian et al. study. Specifically, a control for PTBP1 downregulation was missed in the experiments evaluating astrocyte to neuron conversion *in vivo* (Qian et al., 2020), (Fig. 2b-h and Fig. 3). Although the information pertinent to the *GFAP* promoter in AAV-CasRx plasmids was completely missing in Zhou et al study, the information from Addgene (https://www.addgene.org/154001/ and https://www.addgene.org/154000/) shows that these plasmids comprise a short form *GFAP* promoter. Wang et al, however, was not able to downregulate PTBP1 and hence trigger glia-to-neuron conversion using the same AAV-CasRx system (Wang et al., 2021). In addition, we observed that PTBP1 predominantly localizes in nucleus, a subcellular compartment for RNA-binding proteins, whereas PTPB1 was detected all over the cell without a specific subcellular localization in Zhou et al. study (Zhou et al., 2020).

The definitive aim of neuronal regeneration is to improve, if not completely restore, brain functions deteriorated in neurodegeneration. Synaptic failure, a primary cause for cognitive impairment in AD, ought to be rescued if nascent neurons would be replenished from the resident glia cells. Our results demonstrate that PTBP1 downregulation cannot improve cognitive and synaptic function through any mechanisms including the neuronal regeneration. However, we do not exclude the possibility that PTBP1 downregulation could improve other brain functions such as motor function, which has been shown previously (Qian et al., 2020; Zhou et al., 2020). Future experiments are required to more carefully and in greater details test the strategy targeting PTBP1 in treating neurodegenerative diseases in not only rodents but also primates.

410 **Materials and methods**

411

412 **Key Resource Table**

REAGENT or RESOURCE	SOURCE	IDENTIFIER
Antibodies		
Rabbit polyclonal anti-PTBP1	Thermo Fisher Scientific	Cat# PA5-81297 RRID: AB_2788516
Mouse monoclonal anti-β-actin	ORIGENE	Cat# TA-09
Mouse monoclonal anti-GFAP	Cell Signaling Technology	Cat# 3670S RRID: AB_561049
Mouse monoclonal anti-NeuN	Abcam	Cat# ab104224 RRID: AB_10711040
Mouse monoclonal anti-PSD95	Millipore	Cat# MAB1596 RRID: AB_2092365
Rabbit monoclonal anti-Synaptophysin	Abcam	Cat# ab16659 RRID: AB_443419
Rabbit monoclonal anti-NeuN	Cell Signaling Technology	Cat# 24307 RRID: AB_2651140
Rabbit monoclonal anti-Doublecortin	Cell Signaling Technology	Cat# 4604S RRID: AB_561007
Mouse monoclonal anti-β-Amyloid,1-16 (6E10)	BioLegend	Cat# 803001 RRID: AB_2564653
Mouse monoclonal anti- phospho-Tau (Ser202, Thr205) (AT8)	Thermo Fisher Scientific	Cat# MN1020 RRID: AB_223647
Bacterial and Virus Strains		
Stable 3 (HB101 *E. coli* strain)	Shanghai Weidi Biotechnology	Cat#DL1046M
Chemicals, Peptides, and Recombinant Proteins		
TurboFect Transfection Reagent	Thermo Fisher Scientific	Cat# R0534A
4, 6-diamidino-2-phenylindole (DAPI)	Sigma-Aldrich	Cat# D9542
Polyetherimide (PEI)	Fushenbio	Cat# FSF0001-1G
poly-L-lysine hydrobromide	Sigma-Aldrich	Cat#P6282-5MG
Experimental Models: Cell Lines		
HEK293T	ATCC	Cat# CRL-3216
Experimental Models: Organisms/Strains		
Mouse:C57BL/6J	Xiamen University	N/A

Mouse: 5×FAD: B6SJL-Tg (APPSwFlLon, PSEN1*M146L*L286V)6799Vas/Mmjax	The Jackson Lab	Stock# 034840-JAX RRID: MMRRC_034840-JAX
Mouse: PS19: B6; C3-Tg (Prnp-MAPT*P301S) PS19Vle/J	The Jackson Lab	Stock# 008169 RRID: IMSR_JAX:008169
Oligonucleotides		
Ptbp1-ASO 5′-GGGTGAAGATCCTGTTCAATA-3′	This paper	N/A
Ctrl-ASO 5′-CAACAAGATGAAGAGCACCAA-3′	This paper	N/A
Recombinant DNA		
pAAV-GFAP-mCherry-scramble 5′-ACCTAAGGTTAAGTCGCCCTCG-3′	This paper	N/A
pAAV-GFAP-mCherry-shPtbp1-1 5′-GGGTGAAGATCCTGTTCAATA-3′	This paper	N/A
pAAV-GFAP-mCherry-shPtbp1-2 5′-TGACCTTACAGACCAGAGATTT-3′	This paper	N/A
pAAV-GFAP-mCherry-shPtbp1-3 5′-ACACTATGGTTAACTACTATAC-3′	This paper	N/A
pAdDeltaF6	Addgene	Cat# 112867
pAAV2/9	Addgene	Cat# 112865
Software and Algorithms		
ImageJ	NIH	https://imagej.nih.gov/ij/
GraphPad Prism version 9.0	GraphPad Software	https://www.graphpad.com/

Animals

Wild-type C57BL/6J mice were obtained from the Laboratory Animal Center at Xiamen University. 5×FAD mice (The Jackson Lab: Stock #034840-JAX); PS19 mice (The Jackson Lab: Stock #008169) were obtained from the Jackson Laboratory (Ellsworth, ME, USA) and were backcrossed into the C57BL/6J for 10 generations. Only male mice were used in behavioral tests, while both male and female mice were used in immunohistochemistry. Mice were randomly grouped by genotype and age. Experiments were conducted and analyzed in a double-blind manner. All animal studies were performed according to the protocols approved by the Institutional Animal Care and Use Committee of

Xiamen University.

Isolation and Culture of Primary Mouse Astrocytes

A modified protocol was performed to use (Schildge et al., 2013). Cortical and hippocampal tissues were dissected from P1-P2 pups and dissociated with 0.05% trypsin for 30 min at 37 °C. Tissues were centrifuged for 5 min at 500 g and mechanically dissociated in DMEM/F12 growth media conaining 20% FBS and 1% penicillin/streptomycin. Cells were passed through a 70 μm cell strainer, centrifuged at 500 g for 3 min, and resuspended in the growth media. Cells were plated into 0.1% poly-L-lysine (Sigma-Aldrich, #P6282) coated 175 cm^2 flasks for proliferation. To examine the efficiency of AAV-mediated PTPB1 downregulation *in vitro*, cells were re-plated into 6-well plates, transduced with the AAV and lysed 7 days after the transduction.

Western blot

Western blot was performed as previously described (Zeng et al., 2019). Briefly, primary cultured astrocytes were lysed in RIPA buffer (150 mM NaCl, 50 mM Tris-HCl [pH 8.0], 2 mM EDTA, 1% NP-40, 0.1% SDS, 0.5% sodium deoxycholate) containing protease inhibitor cocktail (Roche, #04693132001). Equal amounts of total proteins (20 μg per sample) from the lysates were resolved by SDS-PAGE. The samples were then probed with the primary antibodies against PTBP1(rabbit; 1:1000; Thermo Fisher Scientific; #PA581297) and β-actin (mouse; 1:5000; ORIGENE; #TA-09), followed by HRP conjugated secondary antibodies against rabbit or mouse IgG (1:5000; Thermo Fisher Scientific; #7074S or #7076S).

Vectors and AAV production

To generate astrocyte specific AAV expression vectors, shRNAs targeting mouse *Ptbp1* or scrambled shRNA was inserted into an AAV vector driven by

453 the 2.2 kb long human *GFAP* promoter (*pAAV-GFAP-mCherry-miR30E*)
454 (VectorBuilder: https://www.vectorbuilder.cn/design/retrieve.html, VB200627-
455 1109ntb). The sequences of shRNA-2 and -3 were obtained from Vectorbuilder
456 (https://www.vectorbuilder.cn/design/pRP_shRNA.html), while shRNA-1
457 sequence was designed based on a recent study (Qian et al., 2020). The target
458 sequences of shRNAs and scramble were as follows: scramble: 5′-ACCTA
459 AGGTT AAGTC GCCCT CG-3′; sh*Ptbp1*-1:5′-GGGTG AAGAT CCTGT TCAAT
460 A-3′; shP*tbp1*-2: 5′-TGACC TTACA GACCA GAGAT TT-3′; sh*Ptbp1*-3: 5′-
461 ACACT ATGGT TAACT ACTAT AC-3′.
462 AAV viruses were produced following a well-established protocol with minor
463 modifications (Challis et al., 2019). Briefly, HEK293T cells (ATCC, #CRL-3216)
464 were transfected with the pAAV-shRNA, pAAV2/9 Helper (Addgene, #112867),
465 and pAd-deltaF6 (Addgene, #112865) plasmids. Three days post transfection,
466 viral particles were collected from the media and lysates of the cells, and
467 purified by iodixanol gradient ultracentrifugation in a Beckman L-100XP
468 centrifuge with type 70 Ti rotor at 350,000g for 2 hours and 25 min at 18 °C.
469
470 **Stereotactic injection**
471 Stereotactic injection was performed as described previously (Wang et al., 2013;
472 Zhao et al., 2015). Briefly, after anesthetization with Avertin, the experimental
473 mice were shaved to remove the head hairs and secured in an automated
474 stereotaxic injection apparatus (RWD Life Science). Ctrl-ASO or *Ptbp1*- ASO
475 (2 μl, 2.5 μg/μL) were injected into the following coordinates: for hippocampal
476 den-tate gyrus. -2.5 mm anteroposterior (AP) from the bregma, ±2.0 mm
477 mediolateral (ML), -2.4 mm dorsoventral (DL); The target sequences of ASO
478 and Ctrl were as follows: PTB-ASO: 5′-GGGTG AAGAT CCTGT TCAAT A-3′;
479 Ctrl-ASO: 5′-CAACA AGATG AAGAG CACCA A-3′; AAV- sh*Ptbp1* or AAV-
480 scramble (2 μl, titer $1x10^{12}$ viral genomes/mL) viruses were injected into the
481 following coordinates: for hippocampal dentate gyrus, -2.5 mm anteroposterior

482 (AP) from the bregma, ±2.0 mm mediolateral (ML), -2.4 mm dorsoventral (DL);
483 for striatum, -0.8 mm AP from the bregma, ±1.6 mm ML, -2.8 mm DV; for
484 substantia nigra, -3.0 mm AP from the bregma, ±1.2 mm ML, -4.6 mm DL.

485

486 **Immunofluorescence**

487 Mice were anesthetized with Avertin followed by intracardial perfusion with PBS
488 and 4% paraformaldehyde (PFA) in PBS. Mouse brains were dissected quickly,
489 post-fixed with 4% PFA overnight at 4 °C, and dehydrated with 30% sucrose in
490 PBS until it completely settled. The brains were then encased in optimal cutting
491 temperature compound (Sakura; #4583), and cut into serial frozen sections (30-
492 40 μm) using a cryostat (Leica; #CM1950). The sections were permeabilized
493 and blocked with PBS containing 0.3% Triton X-100 and 10% normal donkey
494 serum for 45 min at room temperature. The sections were incubated with the
495 following primary antibodies at 4 °C overnight: mouse anti-GFAP (1:500; CST;
496 #3670S), rabbit anti-NeuN (1:500; CST; #24307), mouse anti-NeuN (1:1000;
497 Abcam; #ab104224), rabbit anti-PTBP1 (1:200; Thermo Fisher Scientific; #PA5-
498 81297), rabbit anti-Doublecortin (1:500; CST; #4604S), moues-anti-PSD95
499 (1:100; Millipore; #MAB1596), rabbit anti-Synaptophysin (1:200; Abcam;
500 AB_443419), mouse anti-Aβ (6E10) (1:500; BioLegend; #803001) and mouse
501 anti-Phospho-Tau (Ser202, Thr205) (AT8) (1:200; Thermo Fisher Scientific;
502 #MN1020). Donkey derived secondary antibodies conjugated with Alexa Fluor-
503 488 or -647 (1:500; Thermo Fisher Scientific; #A-11034) (1:500; Thermo Fisher
504 Scientific; #A-31571) were used for fluorescence, and DAPI (1 μg/ml, Sigma-
505 Aldrich, #D9542) was used to counterstain nuclei. Images were captured using
506 a Leica SP8 or Zeiss LSM880 confocal microscope and subjected to
507 quantification with ImageJ software [National Institutes of Health (NIH),
508 https://imagej.nih.gov/ij/]

509

510 **Phospho-Tau examination**

511 The levels of phosphor-Tau (T181) were determined by Single Molecule
512 Immune Detection method (Astrobio).
513
514 **Behavioral tests**
515 **Morris water maze (MWM)**
516 MWM tests were performed in a 1.2 m diameter circular tank filled with opaque
517 water at 22 °C, using a modified protocol (Du et al., 2018). The walls
518 surrounding the tank were marked with bright, contrasting shapes which serve
519 as spatial reference cues. A fixed platform (10 cm diameter) was placed in a
520 selected target quadrant. During training, the platform was submerged and the
521 mice were placed into the maze at one of four points randomly facing the wall
522 of the tank. Mice were allowed to search for a platform for 1 min; if the mice
523 were unable to find the platform, they were gently guided to the platform for 10
524 s. Two trials a day were conducted with a minimum of a 1 hour intertrial interval.
525 On day 6, the hidden platform was removed and probe test was performed.
526 Escape latency to find the platform during training and time spent in target
527 quadrant during probe test was recorded and analyzed by CleverSys
528 TopScanLite (Clever Sys, Reston, VA, USA).
529
530 **Novel object recognition (NOR)**
531 NOR consists of three phases: habituation, training and test (Zhao et al., 2019).
532 On day 1, mice were habituated to an open field box (40cm x 40cm x 40cm) for
533 5 min. On day 2, two same objects were placed in two diagonal corners of the
534 box, and mice were put into the box and explored for 8 min. 24 hours later (day
535 3), one of the object was replaced with a novel object, and then mice were put
536 back to the box and allowed to explore for 8 min. Cumulative time of each
537 mouse spent on exploring each object was recorded by TopScanLite
538 (Clever Sys, Reston, VA, USA). The discrimination index was calculated as the
539 following: discrimination index = novel object exploration time/ (novel object

exploration time + familiar object exploration time).

Contextual fear conditioning (CFC) test

CFC tests were performed based on a modified protocol (Shoji et al., 2014). On day 1, mice were placed into a conditioning box with a metal plate, and allowed to explore the box freely for 2 min as habitation. Thereafter, mice were received a 2 s foot electric shock (0.5 mA) for three times, with a 1 min interval between each time. Mice were left in the box for an additional min after the final electric shock. For the contextual test, mice were re-exposed to the same conditioning box for 5 min, 14 days after training. Time of freezing behavior for each mouse was analyzed by CleverSys FreezeScan (Clever Sys, Reston, VA, USA). Freezing % was calculated as the following: freezing % = (freezing time / total time) during the test – (freezing time / total time) during habitation.

Electrophysiology

For analysis of long-term potentiation (LTP), ex-vivo hippocampal slices were prepared from 10-month-old wild type (WT) and 5×FAD mice at three months post the transduction of AAV-sh*Ptbp1* or AAV-scramble. All the subsequent procedures are same as described previously (Zheng et al., 2021).

Acknowledgements

We thank Baoying Xie, Haiping Zheng, Yixian Gao, Xiang You, Qingfeng Liu and Jingru Huang at Xiamen University for technical assistance.

Funding: This study was supported by grants from National Natural Science Foundation of China (92049202 to HX, 82071213 to YZ), and a start-up funding from Xiamen University to YZ.

Author contributions: TG, HX and YZ conceived and designed the study, TG and XP performed behavioral analysis, XP performed and analyzed electrophysiology experiments, TG, XP, GJ, DZ carried out immunofluorescence staining and confocal analysis, JQ, LS and ZW provided helpful discussion, TG, HX and YZ wrote the manuscript. All authors approved the manuscript.

Competing interests: The authors declare no competing interests.

Data and materials availability: Quantification results are displayed as mean ± SEM. Samples sizes are comparable to those described previously in similar studies (Qian et al., 2020; Wang et al., 2021), although statistical methods were not used to predetermine sample sizes in this study. Details for sample sizes and statistical tests can be found in the figure legends. Statistical analyses were performed with GraphPad Prism software (version 9.0, https://www.graphpad.com/). Differences were assessed by unpaired t tests or one-way ANOVA where appropriate. P values < 0.05 were considered as statistically significant.

References

Challis, R. C., Ravindra Kumar, S., Chan, K. Y., Challis, C., Beadle, K., Jang, M. J., Kim, H. M., Rajendran, P. S., Tompkins, J. D., Shivkumar, K., Deverman, B. E., & Gradinaru, V. (2019). Systemic AAV vectors for widespread and targeted gene delivery in rodents. *Nat Protoc*, *14*(2), 379-414. https://doi.org/10.1038/s41596-018-0097-3

Chen, Y. C., Ma, N. X., Pei, Z. F., Wu, Z., Do-Monte, F. H., Keefe, S., Yellin, E., Chen, M. S., Yin, J. C., Lee, G., Minier-Toribio, A., Hu, Y., Bai, Y. T., Lee,

598 K., Quirk, G. J., & Chen, G. (2020). A NeuroD1 AAV-Based Gene
599 Therapy for Functional Brain Repair after Ischemic Injury through In Vivo
600 Astrocyte-to-Neuron Conversion. *Mol Ther*, *28*(1), 217-234.
601 https://doi.org/10.1016/j.ymthe.2019.09.003
602 Demars, M., Hu, Y. S., Gadadhar, A., & Lazarov, O. (2010). Impaired
603 neurogenesis is an early event in the etiology of familial Alzheimer's
604 disease in transgenic mice. *J Neurosci Res*, *88*(10), 2103-2117.
605 https://doi.org/10.1002/jnr.22387
606 Du, Y., Zhao, Y., Li, C., Zheng, Q., Tian, J., Li, Z., Huang, T. Y., Zhang, W., & Xu,
607 H. (2018). Inhibition of PKCdelta reduces amyloid-beta levels and
608 reverses Alzheimer disease phenotypes. *J Exp Med*, *215*(6), 1665-1677.
609 https://doi.org/10.1084/jem.20171193
610 Fu, H., Rodriguez, G. A., Herman, M., Emrani, S., Nahmani, E., Barrett, G.,
611 Figueroa, H. Y., Goldberg, E., Hussaini, S. A., & Duff, K. E. (2017). Tau
612 Pathology Induces Excitatory Neuron Loss, Grid Cell Dysfunction, and
613 Spatial Memory Deficits Reminiscent of Early Alzheimer's Disease.
614 *Neuron*, *93*(3), 533-541 e535.
615 https://doi.org/10.1016/j.neuron.2016.12.023
616 Gage, F. H. (2019). Adult neurogenesis in mammals. *Science*, *364*(6443), 827-
617 828. https://doi.org/10.1126/science.aav6885
618 Grande, A., Sumiyoshi, K., Lopez-Juarez, A., Howard, J., Sakthivel, B., Aronow,
619 B., Campbell, K., & Nakafuku, M. (2013). Environmental impact on direct
620 neuronal reprogramming in vivo in the adult brain. *Nat Commun*, *4*, 2373.
621 https://doi.org/10.1038/ncomms3373
622 Guo, T., Zhang, D., Zeng, Y., Huang, T. Y., Xu, H., & Zhao, Y. (2020). Molecular
623 and cellular mechanisms underlying the pathogenesis of Alzheimer's
624 disease. *Mol Neurodegener*, *15*(1), 40. https://doi.org/10.1186/s13024-
625 020-00391-7

626 Guo, Z., Zhang, L., Wu, Z., Chen, Y., Wang, F., & Chen, G. (2014). In vivo direct
627 reprogramming of reactive glial cells into functional neurons after brain
628 injury and in an Alzheimer's disease model. *Cell Stem Cell*, *14*(2), 188-
629 202. https://doi.org/10.1016/j.stem.2013.12.001
630 Kalia, L. V., & Lang, A. E. (2015). Parkinson's disease. *Lancet*, *386*(9996), 896-
631 912. https://doi.org/10.1016/S0140-6736(14)61393-3
632 Kempermann, G., Gage, F. H., Aigner, L., Song, H., Curtis, M. A., Thuret, S.,
633 Kuhn, H. G., Jessberger, S., Frankland, P. W., Cameron, H. A., Gould,
634 E., Hen, R., Abrous, D. N., Toni, N., Schinder, A. F., Zhao, X., Lucassen,
635 P. J., & Frisen, J. (2018). Human Adult Neurogenesis: Evidence and
636 Remaining Questions. *Cell Stem Cell*, *23*(1), 25-30.
637 https://doi.org/10.1016/j.stem.2018.04.004
638 Leavitt, B. R., & Tabrizi, S. J. (2020). Antisense oligonucleotides for
639 neurodegeneration. *Science*, *367*(6485), 1428-1429.
640 https://doi.org/10.1126/science.aba4624
641 Lentini, C., d'Orange, M., Marichal, N., Trottmann, M. M., Vignoles, R., Foucault,
642 L., Verrier, C., Massera, C., Raineteau, O., Conzelmann, K. K., Rival-
643 Gervier, S., Depaulis, A., Berninger, B., & Heinrich, C. (2021).
644 Reprogramming reactive glia into interneurons reduces chronic seizure
645 activity in a mouse model of mesial temporal lobe epilepsy. *Cell Stem*
646 *Cell*. https://doi.org/10.1016/j.stem.2021.09.002
647 Liu, Y., Miao, Q., Yuan, J., Han, S., Zhang, P., Li, S., Rao, Z., Zhao, W., Ye, Q.,
648 Geng, J., Zhang, X., & Cheng, L. (2015). Ascl1 Converts Dorsal Midbrain
649 Astrocytes into Functional Neurons In Vivo. *J Neurosci*, *35*(25), 9336-
650 9355. https://doi.org/10.1523/JNEUROSCI.3975-14.2015
651 Maimon, R., Chillon-Marinas, C., Snethlage, C. E., Singhal, S. M., McAlonis-
652 Downes, M., Ling, K., Rigo, F., Bennett, C. F., Da Cruz, S., Hnasko, T.
653 S., Muotri, A. R., & Cleveland, D. W. (2021). Therapeutically viable
654 generation of neurons with antisense oligonucleotide suppression of

655 PTB. *Nat Neurosci*, *24*(8), 1089-1099. https://doi.org/10.1038/s41593-
656 021-00864-y
657 Matsuda, T., Irie, T., Katsurabayashi, S., Hayashi, Y., Nagai, T., Hamazaki, N.,
658 Adefuin, A. M. D., Miura, F., Ito, T., Kimura, H., Shirahige, K., Takeda, T.,
659 Iwasaki, K., Imamura, T., & Nakashima, K. (2019). Pioneer Factor
660 NeuroD1 Rearranges Transcriptional and Epigenetic Profiles to Execute
661 Microglia-Neuron Conversion. *Neuron*, *101*(3), 472-485 e477.
662 https://doi.org/10.1016/j.neuron.2018.12.010
663 Mattugini, N., Bocchi, R., Scheuss, V., Russo, G. L., Torper, O., Lao, C. L., &
664 Gotz, M. (2019). Inducing Different Neuronal Subtypes from Astrocytes
665 in the Injured Mouse Cerebral Cortex. *Neuron*, *103*(6), 1086-1095 e1085.
666 https://doi.org/10.1016/j.neuron.2019.08.009
667 Mesulam, M. M. (1999). Neuroplasticity failure in Alzheimer's disease: bridging
668 the gap between plaques and tangles. *Neuron*, *24*(3), 521-529.
669 https://doi.org/10.1016/s0896-6273(00)81109-5
670 Miller, T., Cudkowicz, M., Shaw, P. J., Andersen, P. M., Atassi, N., Bucelli, R. C.,
671 Genge, A., Glass, J., Ladha, S., Ludolph, A. L., Maragakis, N. J.,
672 McDermott, C. J., Pestronk, A., Ravits, J., Salachas, F., Trudell, R., Van
673 Damme, P., Zinman, L., Bennett, C. F., Lane, R., Sandrock, A., Runz, H.,
674 Graham, D., Houshyar, H., McCampbell, A., Nestorov, I., Chang, I.,
675 McNeill, M., Fanning, L., Fradette, S., & Ferguson, T. A. (2020). Phase
676 1-2 Trial of Antisense Oligonucleotide Tofersen for SOD1 ALS. *N Engl J*
677 *Med*, *383*(2), 109-119. https://doi.org/10.1056/NEJMoa2003715
678 Miller, T. M., Pestronk, A., David, W., Rothstein, J., Simpson, E., Appel, S. H.,
679 Andres, P. L., Mahoney, K., Allred, P., Alexander, K., Ostrow, L. W.,
680 Schoenfeld, D., Macklin, E. A., Norris, D. A., Manousakis, G., Crisp, M.,
681 Smith, R., Bennett, C. F., Bishop, K. M., & Cudkowicz, M. E. (2013). An
682 antisense oligonucleotide against SOD1 delivered intrathecally for
683 patients with SOD1 familial amyotrophic lateral sclerosis: a phase 1,

684 randomised, first-in-man study. *Lancet Neurol*, *12*(5), 435-442.
685 https://doi.org/10.1016/S1474-4422(13)70061-9
686 Niu, W., Zang, T., Smith, D. K., Vue, T. Y., Zou, Y., Bachoo, R., Johnson, J. E.,
687 & Zhang, C. L. (2015). SOX2 reprograms resident astrocytes into neural
688 progenitors in the adult brain. *Stem Cell Reports*, *4*(5), 780-794.
689 https://doi.org/10.1016/j.stemcr.2015.03.006
690 Olanow, C. W., Goetz, C. G., Kordower, J. H., Stoessl, A. J., Sossi, V., Brin, M.
691 F., Shannon, K. M., Nauert, G. M., Perl, D. P., Godbold, J., & Freeman,
692 T. B. (2003). A double-blind controlled trial of bilateral fetal nigral
693 transplantation in Parkinson's disease. *Ann Neurol*, *54*(3), 403-414.
694 https://doi.org/10.1002/ana.10720
695 Perez-Nievas, B. G., & Serrano-Pozo, A. (2018). Deciphering the Astrocyte
696 Reaction in Alzheimer's Disease. *Front Aging Neurosci*, *10*, 114.
697 https://doi.org/10.3389/fnagi.2018.00114
698 Qian, H., Kang, X., Hu, J., Zhang, D., Liang, Z., Meng, F., Zhang, X., Xue, Y.,
699 Maimon, R., Dowdy, S. F., Devaraj, N. K., Zhou, Z., Mobley, W. C.,
700 Cleveland, D. W., & Fu, X. D. (2020). Reversing a model of Parkinson's
701 disease with in situ converted nigral neurons. *Nature*, *582*(7813), 550-
702 556. https://doi.org/10.1038/s41586-020-2388-4
703 Schildge, S., Bohrer, C., Beck, K., & Schachtrup, C. (2013). Isolation and
704 culture of mouse cortical astrocytes. *J Vis Exp*(71).
705 https://doi.org/10.3791/50079
706 Shoji, H., Takao, K., Hattori, S., & Miyakawa, T. (2014). Contextual and cued
707 fear conditioning test using a video analyzing system in mice. *J Vis*
708 *Exp*(85). https://doi.org/10.3791/50871
709 Tai, W., Wu, W., Wang, L. L., Ni, H., Chen, C., Yang, J., Zang, T., Zou, Y., Xu,
710 X. M., & Zhang, C. L. (2021). In vivo reprogramming of NG2 glia enables
711 adult neurogenesis and functional recovery following spinal cord injury.

712 *Cell Stem Cell*, *28*(5), 923-937 e924.
713 https://doi.org/10.1016/j.stem.2021.02.009
714 Torper, O., Ottosson, D. R., Pereira, M., Lau, S., Cardoso, T., Grealish, S., &
715 Parmar, M. (2015). In Vivo Reprogramming of Striatal NG2 Glia into
716 Functional Neurons that Integrate into Local Host Circuitry. *Cell Rep*,
717 *12*(3), 474-481. https://doi.org/10.1016/j.celrep.2015.06.040
718 Trounson, A., & McDonald, C. (2015). Stem Cell Therapies in Clinical Trials:
719 Progress and Challenges. *Cell Stem Cell*, *17*(1), 11-22.
720 https://doi.org/10.1016/j.stem.2015.06.007
721 Wang, L. L., Serrano, C., Zhong, X., Ma, S., Zou, Y., & Zhang, C. L. (2021).
722 Revisiting astrocyte to neuron conversion with lineage tracing in vivo.
723 *Cell*. https://doi.org/10.1016/j.cell.2021.09.005
724 Wang, X., Zhao, Y., Zhang, X., Badie, H., Zhou, Y., Mu, Y., Loo, L. S., Cai, L.,
725 Thompson, R. C., Yang, B., Chen, Y., Johnson, P. F., Wu, C., Bu, G.,
726 Mobley, W. C., Zhang, D., Gage, F. H., Ranscht, B., Zhang, Y. W., Lipton,
727 S. A., Hong, W., & Xu, H. (2013). Loss of sorting nexin 27 contributes to
728 excitatory synaptic dysfunction by modulating glutamate receptor
729 recycling in Down's syndrome. *Nat Med*, *19*(4), 473-480.
730 https://doi.org/10.1038/nm.3117
731 Yoshiyama, Y., Higuchi, M., Zhang, B., Huang, S. M., Iwata, N., Saido, T. C.,
732 Maeda, J., Suhara, T., Trojanowski, J. Q., & Lee, V. M. (2007). Synapse
733 loss and microglial activation precede tangles in a P301S tauopathy
734 mouse model. *Neuron*, *53*(3), 337-351.
735 https://doi.org/10.1016/j.neuron.2007.01.010
736 Zaletel, I., Schwirtlich, M., Perovic, M., Jovanovic, M., Stevanovic, M., Kanazir,
737 S., & Puskas, N. (2018). Early Impairments of Hippocampal
738 Neurogenesis in 5xFAD Mouse Model of Alzheimer's Disease Are
739 Associated with Altered Expression of SOXB Transcription Factors. *J*
740 *Alzheimers Dis*, *65*(3), 963-976. https://doi.org/10.3233/JAD-180277

741 Zeng, F., Ma, X., Zhu, L., Xu, Q., Zeng, Y., Gao, Y., Li, G., Guo, T., Zhang, H.,
742 Tang, X., Wang, Z., Ye, Z., Zheng, L., Zhang, H., Zheng, Q., Li, K., Lu,
743 J., Qi, X., Luo, H., Zhang, X., Wang, Z., Zhou, Y., Yao, Y., Ke, R., Zhou,
744 Y., Liu, Y., Sun, H., Huang, T., Shao, Z., Xu, H., & Wang, X. (2019). The
745 deubiquitinase USP6 affects memory and synaptic plasticity through
746 modulating NMDA receptor stability. *PLoS Biol*, *17*(12), e3000525.
747 https://doi.org/10.1371/journal.pbio.3000525
748 Zhao, D., Meng, J., Zhao, Y., Huo, Y., Liu, Y., Zheng, N., Zhang, M., Gao, Y.,
749 Chen, Z., Sun, H., Wang, X., Jing, C., Zhang, T., Zhang, X., Luo, H.,
750 Wang, X., Zhang, J., Liu, F. R., Li, Y., Bu, G., Wen, L., Huang, T. Y., Xu,
751 H., & Zhang, Y. W. (2019). RPS23RG1 Is Required for Synaptic Integrity
752 and Rescues Alzheimer's Disease-Associated Cognitive Deficits. *Biol*
753 *Psychiatry*, *86*(3), 171-184.
754 https://doi.org/10.1016/j.biopsych.2018.08.009
755 Zhao, Y., Tseng, I. C., Heyser, C. J., Rockenstein, E., Mante, M., Adame, A.,
756 Zheng, Q., Huang, T., Wang, X., Arslan, P. E., Chakrabarty, P., Wu, C.,
757 Bu, G., Mobley, W. C., Zhang, Y. W., St George-Hyslop, P., Masliah, E.,
758 Fraser, P., & Xu, H. (2015). Appoptosin-Mediated Caspase Cleavage of
759 Tau Contributes to Progressive Supranuclear Palsy Pathogenesis.
760 *Neuron*, *87*(5), 963-975. https://doi.org/10.1016/j.neuron.2015.08.020
761 Zheng, Q., Li, G., Wang, S., Zhou, Y., Liu, K., Gao, Y., Zhou, Y., Zheng, L., Zhu,
762 L., Deng, Q., Wu, M., Di, A., Zhang, L., Zhao, Y., Zhang, H., Sun, H.,
763 Dong, C., Xu, H., & Wang, X. (2021). Trisomy 21-induced dysregulation
764 of microglial homeostasis in Alzheimer's brains is mediated by USP25.
765 *Sci Adv*, *7*(1). https://doi.org/10.1126/sciadv.abe1340
766 Zhou, H., Su, J., Hu, X., Zhou, C., Li, H., Chen, Z., Xiao, Q., Wang, B., Wu, W.,
767 Sun, Y., Zhou, Y., Tang, C., Liu, F., Wang, L., Feng, C., Liu, M., Li, S.,
768 Zhang, Y., Xu, H., Yao, H., Shi, L., & Yang, H. (2020). Glia-to-Neuron
769 Conversion by CRISPR-CasRx Alleviates Symptoms of Neurological

770 Disease in Mice. *Cell*, *181*(3), 590-603 e516.
771 https://doi.org/10.1016/j.cell.2020.03.024
772